

# DYNAMICAL EFFECTS OF NUCLEAR RINGS IN DISK GALAXIES

Clayton H. Heller  
Universitäts Sternwarte  
Geismarlandstraße 11  
D-37083 Göttingen, Germany  
Email: cheller@uni-sw.gwdg.de

and

Isaac Shlosman  
Department of Physics and Astronomy  
University of Kentucky  
Lexington, KY 40506-0055, USA  
Email: shlosman@asta.pa.uky.edu

## ABSTRACT

We investigate the dynamical response of stellar orbits in a rotating barred galaxy potential to the perturbation by a nuclear gaseous ring. The change in 3D periodic orbit families is examined as the gas accumulates between the inner Lindblad resonances. It is found that the phase space allowable to the  $x_2$  family of orbits is substantially increased and a vertical instability strip appears with the growing mass of the ring. A significant distortion of the  $x_1$  orbits is observed in the vicinity of the ring, which leads to the intersection between orbits with different values of the Jacobi integral. We also examine the dependence of the orbital response to the eccentricity and alignment of the ring with the bar. Misalignment between an oval ring and a bar can leave observational footprints in the form of twisted near-infrared isophotes in the vicinity of the ring. It is inferred that a massive nuclear ring acts to weaken and dissolve the stellar bar exterior to the ring, whereas only weakly affecting the orbits interior to the inner Lindblad resonances. Consequences for gas evolution in the circumnuclear regions of barred galaxies are discussed as well.

*Subject headings:* galaxies: active — galaxies: evolution — galaxies: kinematics and dynamics — galaxies: starburst — galaxies: structure

## 1. INTRODUCTION

It is generally agreed that barred disk galaxies experience radial inflows of the interstellar medium (ISM) (e.g. Kenney 1996, and refs. therein). These flows are presumably triggered by gravitational torques from non-axisymmetric background potentials, such as stellar bars and ovals. (For a more comprehensive discussion of this phenomenon see review by Shlosman, Begelman & Frank 1990). A large fraction,  $\sim 2/3$ , of disk galaxies are observed to be barred to various degrees (e.g. de Vaucouleurs 1963), the remaining 1/3 typically consist of edge-on galaxies where bars would be difficult to detect (e.g. review by Martinet 1995). In addition, most galactic disks are ovals distorted (Bosma 1981; Kormendy 1982; Rix & Zaritsky 1995), especially in the central regions where triaxial stellar bulges are frequent (Kormendy 1993).

Theoretical studies of gaseous inflows confirm that gas can reach the circumnuclear regions of disk galaxies (e.g. Combes and Gerin 1985; Shlosman, Frank & Begelman 1989; Athanassoula 1992; Friedli and Benz 1993; Shlosman and Noguchi 1993) and cause enhanced star formation there, so-called nuclear starbursts (Heller and Shlosman 1994; Knapen et al. 1995a). Indeed, observations of nuclear starburst galaxies reveal ring-like molecular gas accumulations within the central kpc (e.g. Telesco and Decher 1988; Pogge 1989; Kenney et al. 1992; Benedict et al. 1993; Knapen et al. 1995b), where a slowdown of radial inflow is expected in the presence of inner Lindblad resonance(s) (ILRs) (Combes & Gerin 1985; Shlosman, Frank & Begelman 1989). Nuclear rings are ovals shaped and their major axes are observed to lead the stellar bars, typically by  $\sim 50^\circ - 90^\circ$  in the direction of galactic rotation. Frequently, they are patchy and incomplete (Buta & Crocker 1993). A substantial fraction,  $\sim 10\% - 30\%$ , of the molecular galactic ISM can accumulate in these rings, which consist of a mixture of neutral and ionized, gas and dust, and is accompanied by massive star formation. Ring masses can be roughly estimated using the axisymmetric rotation curve and/or emission from this gas. Typical masses range from  $\text{few} \times 10^8 M_\odot$  to  $\text{few} \times 10^9 M_\odot$ , and even higher (Kenney 1996 and refs. therein). Besides being an active site of star formation, a nuclear ring provides a significant gravitational perturbation to the background galactic potential, and is expected to alter the main stellar and gas orbits in the central regions. Growing molecular rings further contribute to the increased mass concentration in the disk. Because of this we expect them to modify the inner galactic rotation curve and the positions and strength of the ILRs.

Previous studies of stellar orbits in a rapidly rotating barred potential focused on the secular effects of a growing *spherically-symmetric* central mass concentration, e.g. massive black hole and/or galactic bulge, exceeding  $10^9 M_\odot$ , or  $\sim 1\%$  of the overall mass of a galaxy (Martinet & Pfenniger 1987; Hasan & Norman 1990; Hasan, Pfenniger & Norman 1993). In particular, the main 3D periodic orbits in a barred system with a central mass have been identified and their stability analyzed. These studies exposed the crucial role of ILRs and higher-order resonances in increasing the stochasticity in the system, or simply heating it up, which results in the weakening and dissolution of the stellar bar and the buildup of the galactic bulge. This interesting phenomenon has led the authors to argue in favor of galaxy evolution along the Hubble sequence

(Pfenniger, Combes and Martinet 1994; Martinet 1995). Implications for gas dynamics have been studied by Pfenniger & Norman (1990) neglecting the self-gravity in the gas.

Although it is possible that all nuclear starburst galaxies (and even all disk galaxies!) harbor central black holes (BHs), it is by no means clear that the masses of these BHs are in the range of  $\gtrsim 10^9 M_\odot$ . It is plausible that typical BHs in disk galaxies, active and normal, are much less massive, and lie in the mass range of  $\sim 10^7 - 10^8 M_\odot$  (with the exception of quasar hosts). For example, Emmering, Blandford and Shlosman (1992) have argued that BHs in Seyfert nuclei may be more efficient in extracting energy and angular momentum from the accreting material than commonly believed, allowing for lower estimates of BH masses there. On the other hand, a buildup of galactic bulges may proceed on a timescale which is a fraction of a Hubble time and cause the same effects on the galactic dynamics within the bar region, as discussed in the previous paragraph.

Evidently, the estimated masses of nuclear rings make them competitive with galactic bulges in affecting the structure of disk galaxies. At the same time, their morphology differs quite dramatically from that of nearly spherically-symmetric or weakly triaxial bulges. This motivated us to analyze the main periodic orbits in a barred potential perturbed by a growing nuclear ring. We aim at understanding the gravitational effects of this phenomenon on the stellar orbits, as well as deduce possible implications on the gas evolution in these galaxies. Both circular and oval rings are used, and the results are compared to the previous studies of such orbits, with and without the central mass (e.g. Contopoulos & Papayannopoulos 1980; Athanassoula et al. 1983; Pfenniger 1984; Hasan, Pfenniger & Norman 1993). We find that in many ways, the dynamical consequences of nuclear rings differ from those of a spherically-symmetric central mass, as addressed so far in the literature.

In the next section we describe a model for the background galactic potential, which is perturbed by a massive ring. The potential of an elliptical hoop, representing the ring, is calculated analytically. The third section presents the method we employ to locate the main families of periodic orbits in the phase space. Readers that wish to avoid the technical details may go directly to the fourth section, where the results of the orbital analysis are given for a series of circular and elliptical ring models, with gradually increasing mass and different orientations with respect to the stellar bar. A discussion of the possible effects on the gas flow in a galaxy is given in the last section.

## 2. MODEL

The galaxy model consists of the superposition of four components: disk, bulge, bar, and ring. For the disk we choose a potential introduced by Miyamoto and Nagai (1975),

$$\Phi_d = -\frac{GM_d}{\sqrt{R^2 + \left(A_d + \sqrt{B_d^2 + z^2}\right)^2}}, \quad (1)$$

where  $R^2 = x^2 + y^2$ . This axisymmetric potential is characterized by the total mass  $M_d$ , horizontal scale  $A_d + B_d$ , and vertical scale  $B_d$ . When  $B_d = 0$ ,  $\Phi_d$  reduces to Kuzmin's very flattened potential. For the spherically symmetric bulge or spheroidal component we will use a Plummer sphere,

$$\Phi_s = -\frac{GM_s}{\sqrt{R^2 + z^2 + B_s^2}}. \quad (2)$$

The bar is represented by a triaxial Ferrers (1877) density distribution of semi-axes  $a$ ,  $b$ , and  $c$ , given by

$$\rho = \begin{cases} \frac{105M_b}{32\pi abc} (1 - m^2)^2 & \text{if } m < 1 \\ 0 & \text{if } m \geq 1, \end{cases} \quad (3a)$$

where

$$m^2 = \frac{x^2}{a^2} + \frac{y^2}{b^2} + \frac{z^2}{c^2} \quad (3b)$$

and  $a > b > c$ . We have adopted the strict inequality, rather than use a prolate distribution, because of the desire to represent an intermediate strength bar of moderate eccentricity, as is observed in many of the galaxies which are known to contain nuclear rings of gas. We use the technique of Pfenniger (1984) to evaluate the corresponding potential.

The ring is represented by the fully 3D softened potential of a uniform density elliptical curve in the disk plane of linear density  $\lambda$ , as given by,

$$\Phi_r = -G\lambda \int \frac{ds}{d}, \quad (4)$$

where  $d$  is the distance between a point on the ring  $[r, \phi, 0]$  and the point of evaluation  $[R, \theta, z]$ . With the functions

$$g(\phi) = \sqrt{\frac{1 - e^2}{1 - e^2 \cos^2 \phi}} \quad (5a)$$

and

$$f(\phi) = \frac{e^2 \sin \phi \cos \phi}{1 - e^2 \cos^2 \phi}, \quad (5b)$$

the potential can be written as

$$\Phi_r = -G\lambda R_0 \int_{\theta}^{\theta+2\pi} \frac{g(\phi) \sqrt{1 + f(\phi)^2} d\phi}{\sqrt{R^2 + z^2 + R_0^2 g(\phi)^2 - 2RR_0 g(\phi) \cos(\phi - \theta) + \epsilon^2}}, \quad (6)$$

where  $R_0$  is the semi-major axis,  $e$  the ellipticity, and  $\epsilon$  a softening parameter which gives the ring an effective thickness. Expanding the integrand in  $e$  to second order and substituting  $\phi = \pi - 2\psi + \theta$  gives,

$$\Phi_r = -G\lambda R_0 \int_0^{\pi/2} \left[ \frac{C_0}{\Delta} + e^2 \frac{C_1 + C_2 \cos^2 \psi + C_3 \cos^4 \psi + C_4 \cos^6 \psi}{\Delta^3} + O(e^4) \right] d\psi, \quad (7)$$

where,

$$\Delta = \sqrt{1 - k^2 \sin^2 \psi}, \quad (8a)$$

$$k = \sqrt{1 - k'^2}, \quad (8b)$$

$$k' = R_1/R_2, \quad (8c)$$

$$R_1^2 = (R - R_0)^2 + z^2 + \epsilon^2, \quad (8d)$$

$$R_2^2 = (R + R_0)^2 + z^2 + \epsilon^2, \quad (8e)$$

and the coefficients, which depend only on the point of evaluation, are given by

$$C_0 = -4, \quad (9a)$$

$$C_1 = (2R_0x^2R - 2R^3R_0 - 2\epsilon^2x^2 + 2R^4 + 2z^2R^2 - 2x^2R^2 - 2z^2x^2 + 2\epsilon^2R^2)/R^2, \quad (9b)$$

$$C_2 = -(8R^4 + 8\epsilon^2R^2 - 16\epsilon^2x^2 + 8z^2R^2 - 12R^3R_0 - 16z^2x^2 - 16x^2R^2 + 20R_0x^2R)/R^2, \quad (9c)$$

$$C_3 = (-16z^2x^2 - 16x^2R^2 + 8R^4 - 16\epsilon^2x^2 + 8z^2R^2 - 24R^3R_0 + 48R_0x^2R + 8\epsilon^2R^2)/R^2, \quad (9d)$$

$$C_4 = -\frac{16R_0(2x^2 - R^2)}{R}. \quad (9e)$$

This may now be integrated using standard integral tables to give

$$\Phi_r = \frac{G\lambda R_0}{R_2} \left[ C_0 I_0 + \frac{e^2}{R_2^2} (C_1 I_1 + C_2 I_2 + C_3 I_3 + C_4 I_4) + O(e^4) \right], \quad (10)$$

with,

$$I_0 = K(k), \quad (11a)$$

$$I_1 = E(k)/k'^2, \quad (11b)$$

$$I_2 = \frac{K(k) - E(k)}{k^2}, \quad (11c)$$

$$I_3 = \frac{(k'^2 + 1)E(k) - 2k'^2 K(k)}{k^4}, \quad (11d)$$

$$I_4 = \frac{(2k'^2 - 4k'^2)I_3 + 3k'^2 I_2}{3k^2}, \quad (11e)$$

where  $K$  and  $E$  are the complete elliptic integrals of the 1st and 2nd kinds, respectively.

For  $e = 0$  the above expression reduces to the the 3D potential of a circular hoop. Substituting  $M_r = 2\pi\lambda R_0$  this gives

$$\Phi_{\text{hoop}} = -\frac{2GM_r}{\pi R_2}K(k) \quad (12)$$

and can be compared with the derivation by MacMillan (1958). The full expression has been checked against an numerical integration of Equation 6.

For the model parameters we have chosen values of  $M_d = 1.7$ ,  $A_d = 0.5$ ,  $B_d = 0.05$ ,  $M_s = 0.1$ ,  $B_s = 0.05$ ,  $M_b = 0.12$ ,  $a = 0.5$ ,  $b = 0.25$ ,  $c = 0.05$ ,  $R_0 = 0.04$ , and  $\epsilon = 0.01$ . With adopted units for mass and distance of  $M = 10^{11} M_\odot$  and  $R = 10$  Kpc, respectively, this model has a mass within 10 Kpc of approximately  $1.1 \times 10^{11} M_\odot$ . The bar of length 5 Kpc and axial ratios  $b/a = 0.5$  and  $c/a = 0.1$ , represents about 22% of the mass within its radius. The center of the ring is at a radius (or a semi-major axis) of  $R_0 = 400$  pc in the disk plane and is smeared by the softening so that about 60% of its mass is contained in a cylindrical shell of 200 pc in radius and height centered at  $R_0$ . This was done to avoid singular forces at the position of the ring. We will examine models with ring masses of 0.0,  $10^8$ ,  $5 \times 10^8$ , and  $10^9$  solar masses, which are added to the mass of the system. Because the mass of the ring is insignificant compared to the overall mass, and because the system itself is not dynamically self-consistent, this is the simplest way to account for the gas accumulation in the ring. These rings represent, respectively, 0, 6, 23, and 38 percent of the mass inside the cylindrical shell (for circular rings). The bar pattern speed was chosen for the corotation to be at the end of the bar, which gives  $\Omega_p = 2.284$ . Two radial (and one vertical) ILRs exist at this value of  $\Omega_p$ , as discussed in Section 4. The first four models (A–D) have either none or a circular ring ( $e = 0$ ), the next three (E–G) have an elliptical ring ( $e = 0.4$ ) with varying position angles with respect to the x-axis ( $\alpha$ ). The parameters of these models are given in Table 1.

The surface density produced by model A which has no ring is shown in Figure 1. Because of the small dense central region, the rotation curve of the azimuthally averaged mass distribution rises steeply to about 180 Km/s at 500 pc, followed by a more gentle rise to 240 Km/s at 6 Kpc.

Model	$M_r$	$e$	$\alpha$
A	0.0	0.0	–
B	$10^8$	0.0	–
C	$5 \times 10^8$	0.0	–
D	$10^9$	0.0	–
E	$10^9$	0.4	0
F	$10^9$	0.4	60
G	$10^9$	0.4	90

Table 1: Model Parameters

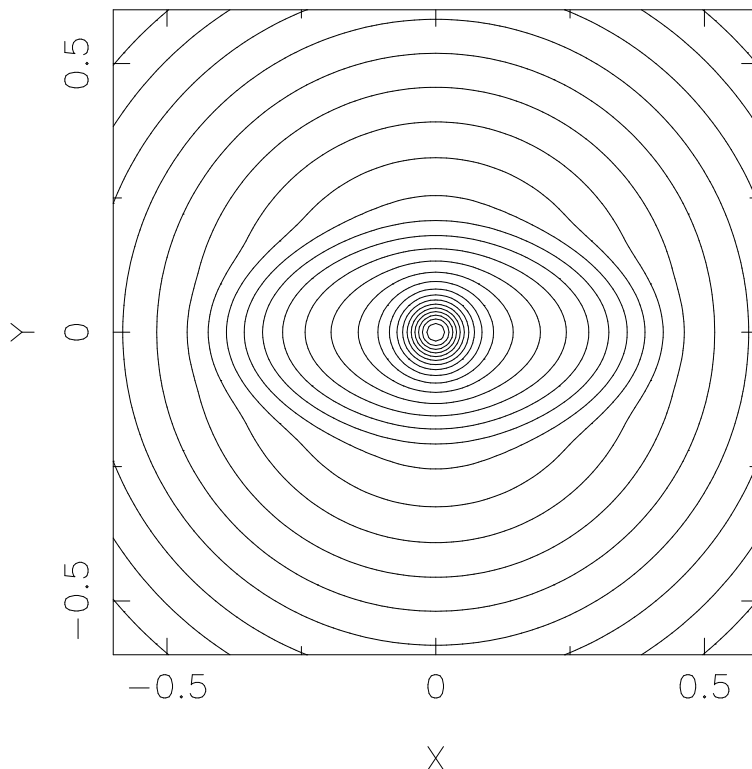


Fig. 1.— Surface density of model without nuclear ring. Each contour represents a change in density of 20%. The frame is 12 Kpc on a side.

### 3. METHOD

We determine the dynamical consequences of the nuclear ring on stars and gas by studying the orbits that are supported by the potential. The backbone of an orbital analysis are the periodic orbits, i.e. orbits which make a closed figure in a frame of reference that rotates with the bar. Since most orbits in a galactic like potential are not periodic, one may ask what is the importance of these, rather special orbits. The answer is that the periodic orbits can be used to characterize the overall orbital structure of phase space. Each periodic orbit traps a region of phase space around it, so that nearby orbits within the region trapped will remain nearby. Trapped orbits generally will have a similar shape to its parent periodic orbit. Such orbits are referred to as being regular, while orbits which are not trapped around any periodic orbit, are referred to as being irregular or ergodic, and are free to move throughout the non-regular regions, at least within energy considerations.

It should also be noted that in a rotating frame of reference neither the energy nor the angular momentum are conserved. There is however an integral of motion, known as the Jacobi Integral. This integral of motion, which remains constant along any given orbit, can be thought of as an effective energy.

To locate the periodic orbits we systematically search the phase space  $\mathbf{y}_0 = \{x_1, x_2, x_3, \dot{x}_1, \dot{x}_2, \dot{x}_3\}$ , by computing orbits with a given Hamiltonian and starting on a particular plane  $x_i = 0$  with sign  $\dot{x}_i$ . The Hamiltonian, given in this case by the Jacobi energy  $E_J$ , is used to eliminate the momentum conjugate to  $x_i$ , leaving four degrees of freedom for the initial conditions. The trajectory is then computed, in the rotating frame of the bar, until it again crosses the plane  $x_i = 0$  with the same sign as  $\dot{x}_i$ , giving phase space coordinates  $T(\mathbf{y}_0) = \mathbf{y}_1$ . The periodic orbits given by the fixed points of the map  $T(\mathbf{y}_0) = \mathbf{y}_0$  are then computed by an iterative procedure based on the numerically determined Jacobian  $\nabla T$ . For this the least-squares method described by Pfenniger and Friedli (1993) is used. Further details on finding periodic orbits may also be found in this reference.

Since the Jacobian  $\nabla T$  is a linear approximation of the phase space around  $\mathbf{y}_0$ , i.e.

$$T(\mathbf{y}_0 + \Delta\mathbf{y}) = T(\mathbf{y}_0) + \nabla T \cdot \Delta\mathbf{y} + O(\|\Delta\mathbf{y}\|^2), \quad (13)$$

its eigenvalues provide information on the stability of the periodic orbit. For convenience, two stability coefficients based on these eigenvalues are defined, such that the orbit is stable if both are real and less than or equal to two in absolute value (Pfenniger 1984). For planar orbits, the eigenvectors have fixed directions, and the stability coefficients may be identified with the horizontal ( $b_H$ ) and vertical ( $b_V$ ) stability of the orbit.

The orbits are computed using a 13 stage embedded Runge-Kutta formula of order 8/7 with adaptive step size (Prince & Dormand 1981). The trajectories are computed with a relative accuracy of  $10^{-14}$ . The program uses the Parallel Virtual Machine (PVM) software package to distribute the computation over multiple processors. The parallelization algorithm features dynamical load balancing and is robust against the loss of machines. Both of these features are accomplished by the use of a circular queue implemented by a link list. Each energy to be searched is inserted into the queue. Each slave process searches one energy at a time, requesting an additional energy from the master process as needed. As the master process gives out an energy to a slave the pointer to the head of the queue is advanced. Because of its circular nature this effectively moves the energy to the back of the queue. As the number of energies in the queue becomes smaller than the number of slaves the same energy may be given out more than once. An energy is only removed from the queue when a slave has successfully completed the search at that energy and returned to the master any results. The full search is complete when the queue is empty. For this study eight Dec-Alpha workstations were used.

We start by first locating all the low order periodic orbits in the disk plane and determine the sections along the families which are vertically unstable. For each of these vertical instability strips we search for bifurcating vertical orbits. Once a vertical orbit has been located, its family is followed by predicting the phase space position of subsequent orbits using a fourth order backward divided differences polynomial with variable step size.



## 4. RESULTS OF ORBITAL ANALYSIS

### 4.1. Without a Nuclear Ring

We start by locating the low-order planar periodic families inside corotation when no ring is present. The search is restricted to simple periodic orbits with initial conditions of  $x = \dot{y} = z = \dot{z} = 0$ . The characteristic diagram is shown in Figure 2. This figure shows the Jacobi energy,  $E_J$ , and the value of the crossing point  $y$ , perpendicular to the bar, for each periodic orbit located. The zero velocity curve which delineates the accessible region in the plane is denoted by the symbol ZVC. While each point in this diagram represents a single periodic orbit, a quick glance shows that it is not covered uniformly by points, but that the periodic orbits define curves in this plane. Hence, the orbits are not unrelated, but fall into families, with each family being defined by its characteristic curve. Sections of the characteristics where the orbits are stable are represented with a solid line, while unstable sections are broken.

The main families in this diagram have been labeled using the notation of Contopoulos and Papayannopoulos (1980). The  $x_1$  family are orbits elongated along the bar and rotate about the center in the same sense as the bar (direct). In the frame of reference of the bar, they also move radially in and out, twice for once around the center (2/1). It is the population of these orbits that predominantly defines the bar, giving it its shape and structure.

The x-extent (along the bar) of the  $x_1$  family increases monotonically with increasing energy from the center out to the 3/1 bifurcation, while the y-extent has a local maximum at  $E_J = -5.70$ . Due to the moderately weak bar, the  $x_1$  family orbits have no loops at the ends. The eccentricity also increases monotonically from the center, but only until  $E_J = -4.80$  where it has reached a maximum value of 0.97, and the x-extent of the orbits is about 1.1 Kpc. Further out, the eccentricity of  $x_1$  orbits stays almost constant, and then declines sharply just before the corotation radius. At an energy of  $E_J = -3.54$  the  $x_1$  sequence turns downward and changes to 4/1. In principle, this section of the characteristic is no longer the  $x_1$  orbits as designated by the notation of Contopoulos, which continues to higher energies following a large gap. The 4/1 sequence changes from direct to retrograde at  $E_J = -3.23$ , and then 3-periodic at  $E_J = -3.63$ , before meeting the retrograde family  $x_4$ . This sequence is simpler than the one studied by Pfenniger (1984) because of the lack of an elbow feature, but is very similar to that described by Athanassoula et al (1983).

The family  $x_2$  are direct orbits elongated perpendicular to the bar and their presence is indicative of a ILR(s) in the nonlinear regime (van Albada & Sanders 1982). The characteristic covers a range in energy from  $E_J = -5.24$  to  $-4.88$  along which the y-extent of the orbits increases monotonically from 0.59 to 0.88 Kpc, while the x-extent goes from 0.33 Kpc to a local maximum of 0.46 Kpc at  $E_J = -4.94$ . These four points may be used to define the position of a double radial ILR along each axis. As usually, the  $x_2$  orbits are more rounded than the  $x_1$  orbits, with the eccentricity increasing towards higher energies. The  $x_3$  family are also direct orbits elongated perpendicular to the bar, but are everywhere horizontally unstable.

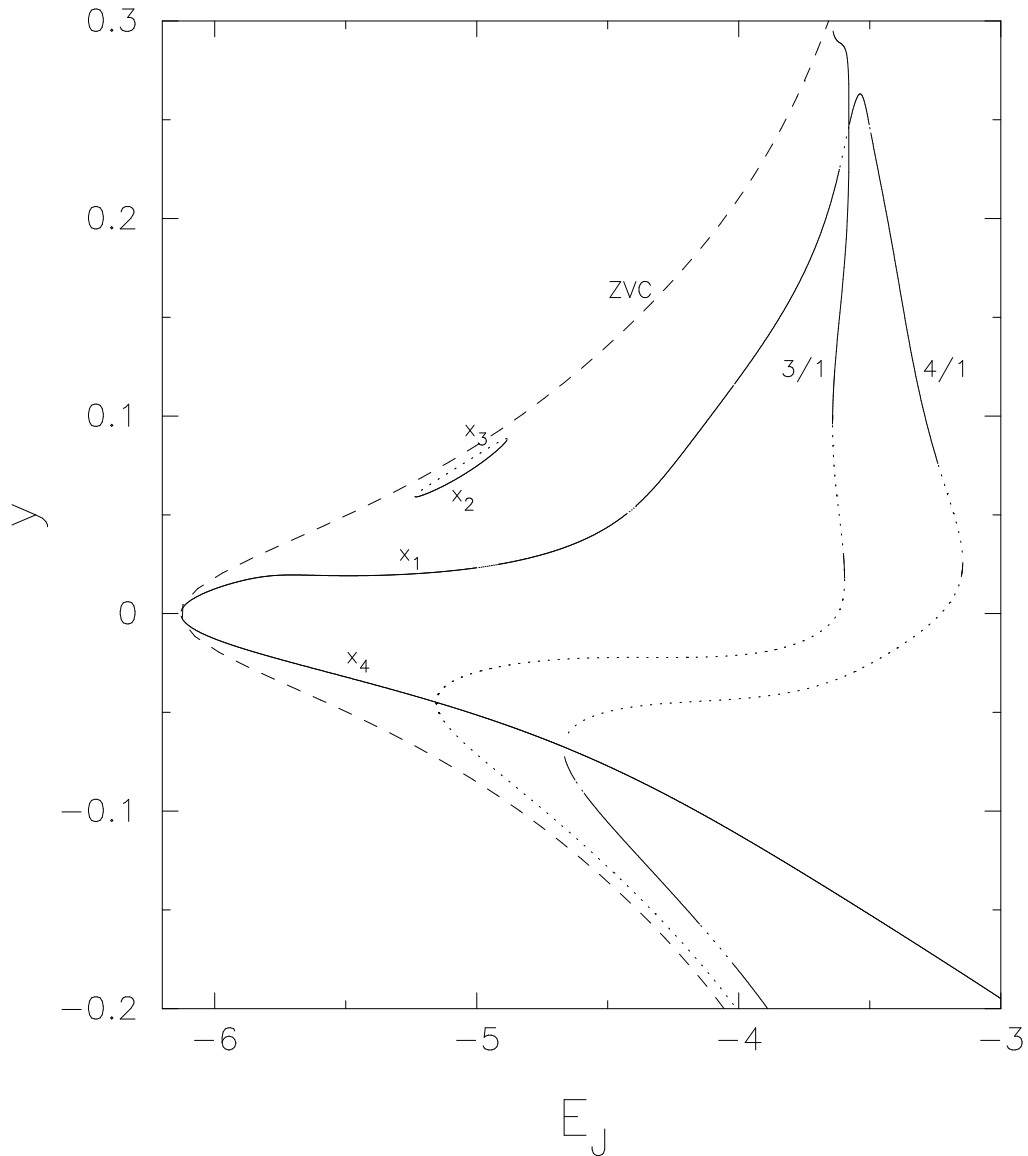


Fig. 2.— Characteristic diagram for planar simple periodic orbits inside corotation when no ring is present. The main families have been labeled: direct ( $x_1$ ) and retrograde ( $x_4$ ) orbits elongated along the bar; ( $x_2$ ) and ( $x_3$ ) direct orbits elongated perpendicular to the bar. The dashed curve labeled ZVC is the zero velocity curve. Stable sections are represented by solid lines while unstable are dotted.

The  $x_4$  family are also 2/1 orbits, but travel in a retrograde sense to the bar and are slightly elongated perpendicular to the bar. For consistency with a bar, this family can only be sparsely populated, as disks with a significant fraction of retrograde orbits are stable to the formation of bars. Likewise, the population of this family during the later stages of evolution can play a role in the dissolution of a bar.

While the  $x_2$ ,  $x_3$ , and  $x_4$  families are vertically stable along their full characteristics, the  $x_1$  family has several sections of vertical instability. We are primarily interested in the two vertically unstable strips at the lowest energies. They can be seen more clearly in the top frame of Figure 3 where they are labeled  $S_1$  and  $S_2$ . In the top left frame of Figure 4 are the stability coefficients for this family. Recalling that a value of  $|b| > 2$  indicates instability, the diagram shows that the two strips are vertically unstable.

Both of these strips,  $S_1$  and  $S_2$ , have two vertical families of orbits bifurcating from them, one in  $z$  and the other in  $\dot{z}$ . Their characteristics are shown in the top frames of Figures 5 and 6. We classify the 3D orbits using the notation of Sellwood and Wilkinson (1993). In this notation  $m:n:l$  implies  $m$  radial oscillations in the  $(x, y)$  plane and  $n$  vertical oscillations in  $z$  as the orbit closes  $l$  rotations about the center. An ‘s’ or ‘a’ subscript is added to indicate whether the orbit is symmetric or anti-symmetric about the  $(y, z)$  plane.

The vertical bifurcation  $V_1$  in  $z$  leads to a family of  $2:2_s:1$  orbits (BAN, i.e. banana-shaped orbits) which are stable from the point of bifurcation at  $E_J = -5.00$  up to  $E_J = -4.88$ , then again between  $E_J = -4.69$  and  $E_J = -4.54$ , after which it remains unstable over the region of interest for this study. The unstable sections shown in Figure 5 are *complex* unstable (see Hasan et al 1993 and refs. therein for discussion of this instability). The vertical bifurcation  $V_2$  in  $z$  at  $E_J = -4.42$  leads to a family of  $2:3_a:1$  orbits which are stable over the entire region of interest. The vertical bifurcations  $V_5$  at  $E_J = -4.92$  and  $V_6$  at  $E_J = -4.39$  in  $\dot{z}$  lead to  $2:2_a:1$  (ABAN, i.e. anti-banana orbits) and  $2:3_s:1$  orbits, respectively, which are unstable everywhere. This situation, where the  $z$  and  $\dot{z}$  bifurcations lead to symmetric and anti-symmetric pairs of orbits, is expected because of the symmetry of the phase space. However, unlike the  $2:2:1$  orbits which are either symmetrical or anti-symmetrical about both the  $(x, z)$  and  $(y, z)$  planes, the  $2:3:1$  orbits are symmetrical with respect to one plane and anti-symmetrical with respect to the other. The  $2:3:1$  orbits are shown in projection and in a “tube” view in Figures 7 and 8.

## 4.2. With a Circular Nuclear Ring

The previous section described the basic orbital structure of model A which contains no nuclear ring. We will now examine the change in the orbital structure when an increasingly massive circular ring is introduced. Position of the ring on the x-axis was chosen as to be between the original ILRs of the Myamoto-Nagai model (0.33 kpc and 0.46 kpc, from extension of  $x_2$  orbits). A circular ring crosses the y-axis interior to the inner ILR. Because the ring is smeared in

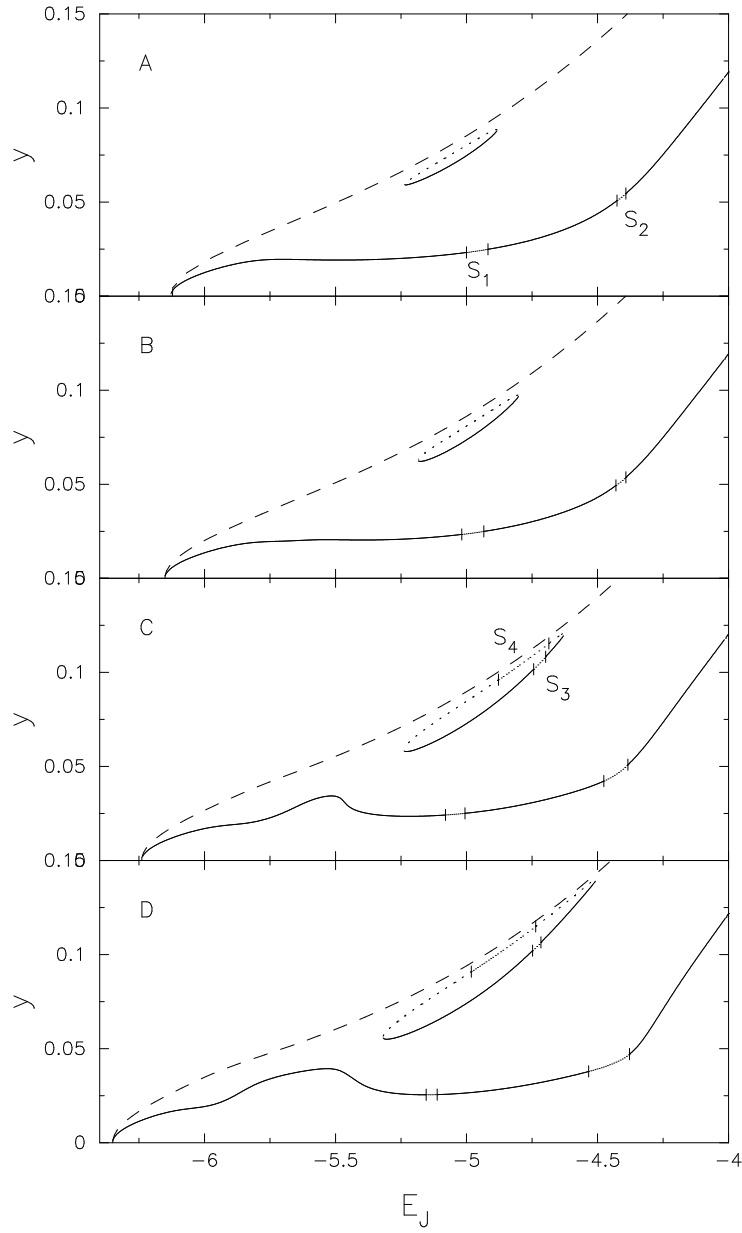


Fig. 3.— Characteristic diagrams of the  $x_1$ ,  $x_2$ , and  $x_3$  families for models with ring mass: (A) 0.0; (B)  $10^8$ ; (C)  $5 \times 10^8$ ; and (D)  $10^9 M_\odot$ . Stable sections of the characteristics are represented by solid lines while unstable are dotted. Four vertical instability strips are marked. The dashed curve is the zero velocity curve.

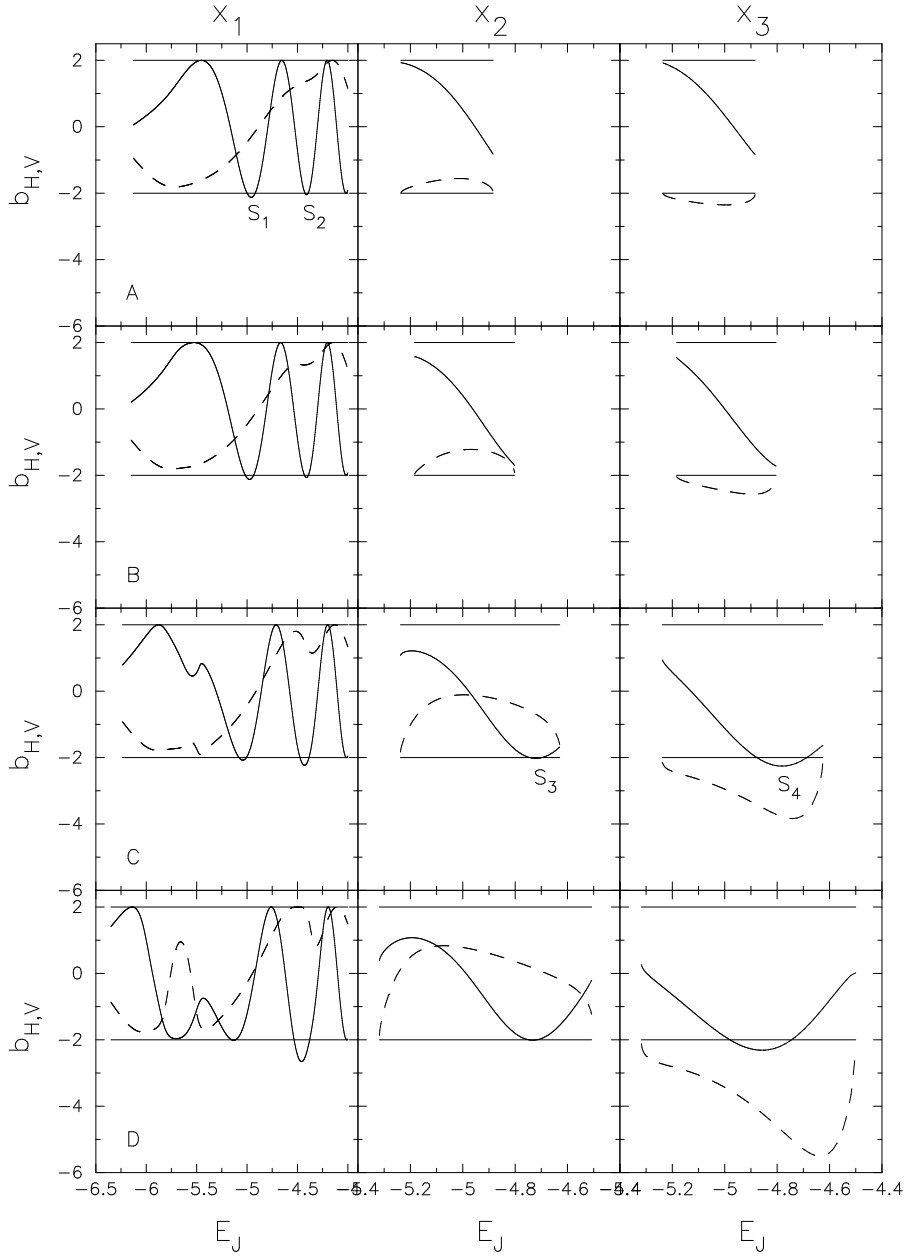


Fig. 4.— Stability diagram showing horizontal coefficient  $b_H$  (dashed) and vertical coefficient  $b_V$  (solid) for the planar periodic orbits of the four models. The stability of the  $x_1$ ,  $x_2$ , and  $x_3$  is shown from left to right. The four vertical instability strips are indicated.

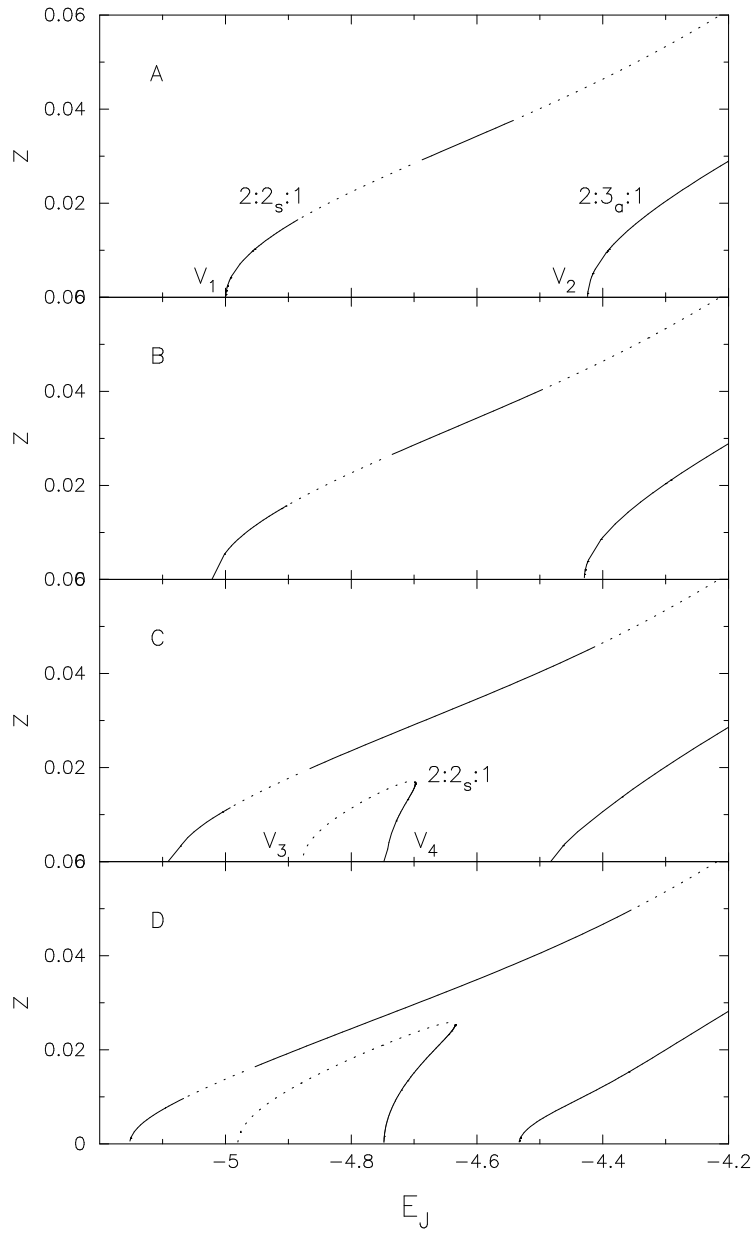


Fig. 5.— Characteristic diagram of vertical orbits bifurcating from the planar instability strips in  $z$ . Stable sections of the characteristic are shown as a solid line while unstable sections are dotted.

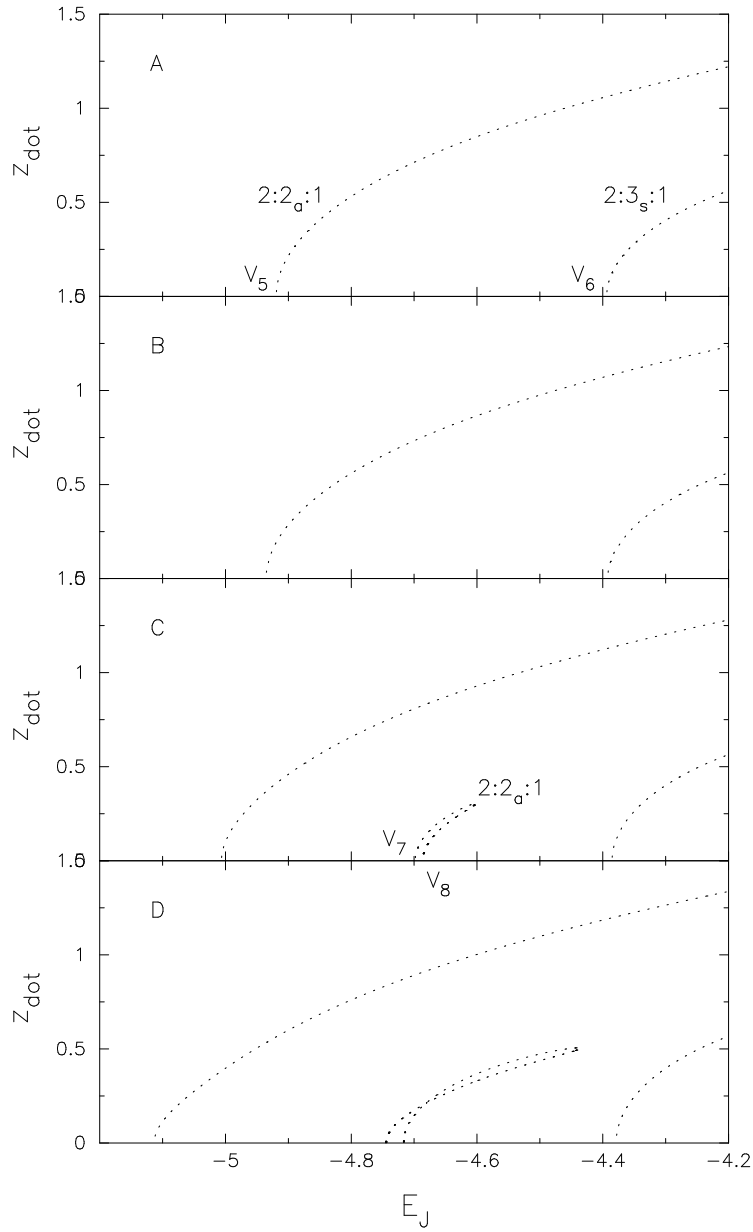


Fig. 6.— Characteristic diagram of vertical orbits bifurcating from the planar instability strips in  $\dot{z}$ . All of the orbits depicted here are unstable.

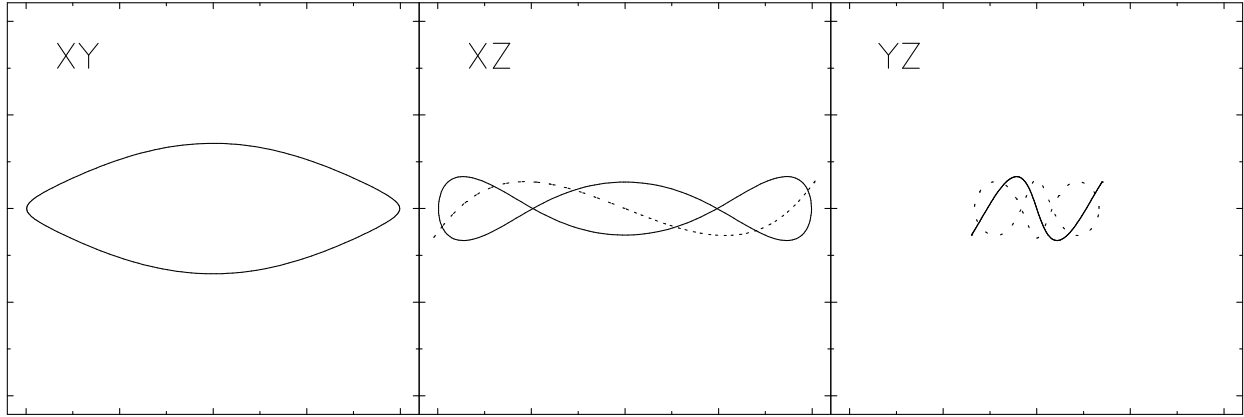


Fig. 7.— Projections onto the three planes of the 2:3:1 symmetric (solid) and anti-symmetric (dashed) 3D orbits.

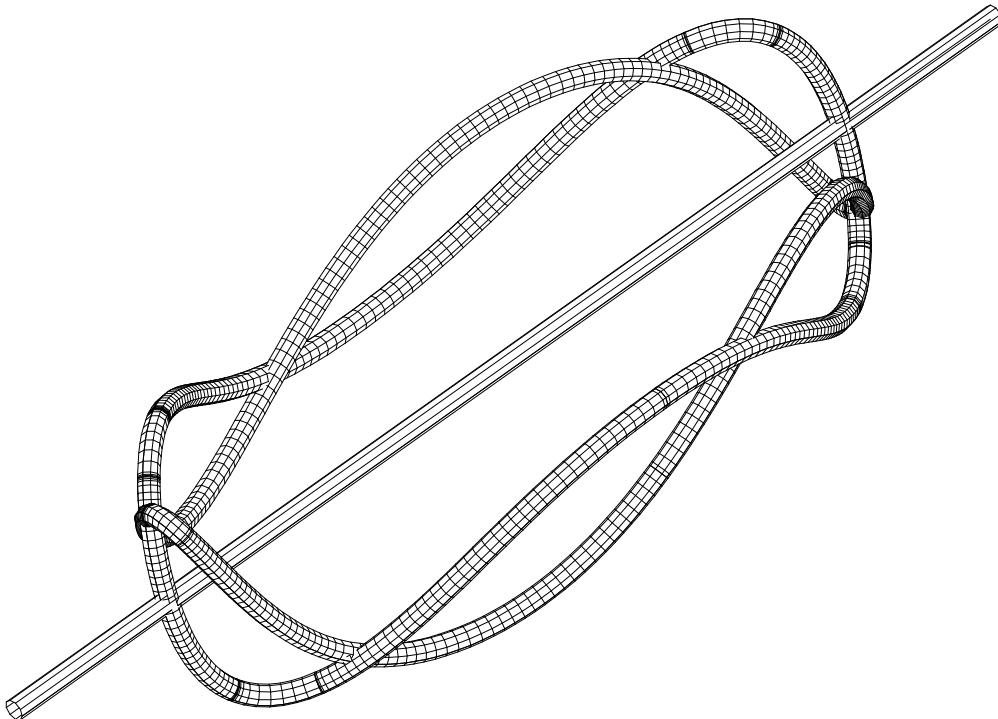


Fig. 8.— Tube view of the 2:3:1 orbits. The x-axis is also indicated.



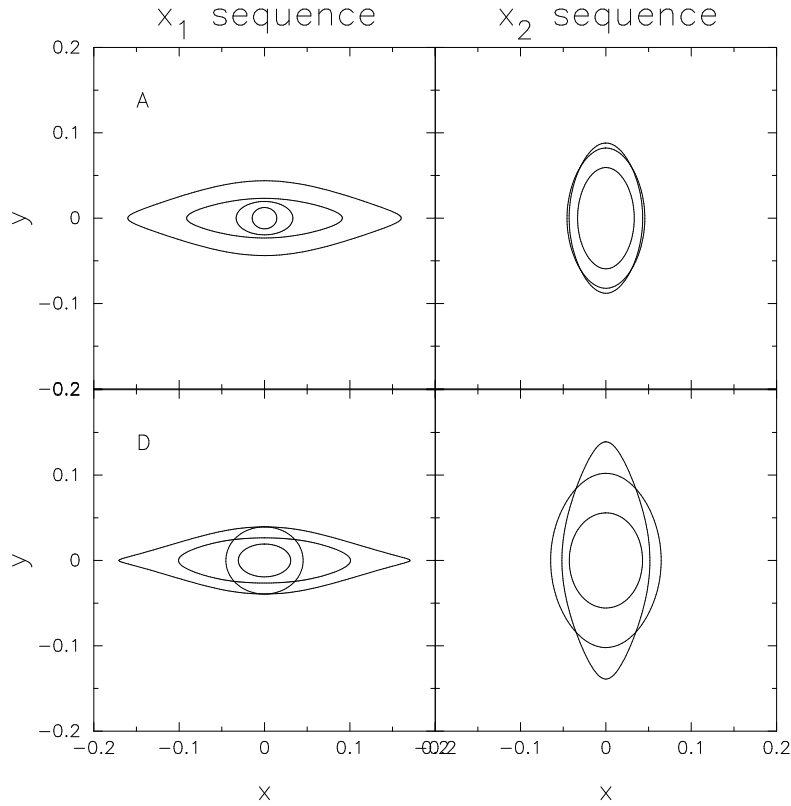


Fig. 9.— Comparison of  $x_1$  and  $x_2$  orbits between the models A and D. For the  $x_1$  orbits  $E_J = -6.0, -5.0, -4.5$ , and the one with maximum  $y$ -extent in the “bump” is shown. For the  $x_2$  orbits the minimum and maximum energy, along with the orbit of maximum  $x$ -extent is shown.

the radial direction, it actually fills up all the space between the ILRs.

The strongest effect observed with the growth of the ring (Fig. 3) is that the extent in energy covered by the  $x_2$  and  $x_3$  orbits increases as the ring mass increases. Previous studies have shown such behavior when the bar is weakened (e.g. Contopoulos & Papayannopoulos 1980). In the present study, where the  $x_1$  family of orbits exists also interior to the ring, the bar is further weakened by a developing and widening shoulder (“bump”) around  $E_J \approx -5.50$ , in the vicinity of the ring. This “bump” is responsible for  $x_1$  orbits becoming rounder near the inner ILR. A comparison of the  $x_1$  and  $x_2$  orbits in the models A and D can be seen in Figure 9. The development of the “bump” produces a significant local maximum in the  $y$ -extent of the  $x_1$  orbits, while the  $x$ -extent continues to increase monotonically with increasing energy. This causes the  $x_1$  orbits in the presence of a massive ring, e.g. in model D, between  $E_J = -5.53$  and  $-4.50$ , or equivalently of 0.45 to 1.7 Kpc  $x$ -extent, to intersect with  $x_1$  orbits of lower energy. Similarly the local maximum in  $x$ -extent along the  $x_2$  sequence causes the orbits with  $E_J = -4.75$  to  $-4.50$ , or 0.65 to 0.52 Kpc  $x$ -extent, to intersect with lower energy  $x_2$  orbits. Due to the  $x_2$  orbits being rounder than the  $x_1$  orbits, they are less distorted and start to intersect at larger ring masses.

As the ring mass is increased, the instability strip  $S_1$  shrinks while at the same time shifting to lower energies. In contrast the instability strip  $S_2$  grows in size toward lower energies. This can be seen more clearly in Figure 4 where the increasing ring suppresses  $S_1$  while enhancing  $S_2$ . For the two higher mass models C and D, vertical instability strips  $S_3$  and  $S_4$  form, respectively, in the  $x_2$  and  $x_3$  sequences, which is rather unusual, as the  $x_2$  orbits are typically stable. The only case of instability strips on  $x_2$  orbits connected by vertical bifurcations was reported by Udry (1991) for slowly rotating triaxial systems. There is only remote similarity between the latter and our case, in that the instability appears in highly flattened systems with  $c/a < 0.3$ . However, contrary to our case, Udry’s bifurcations connect two instability strips on the same  $x_2$  sequence.

From Figures 5 and 6, we see that the vertical bifurcation points  $V_1$ ,  $V_2$ , and  $V_5$  on the  $x_1$  sequence shift to lower energies as the ring increases, while  $V_6$  barely moves. This is in agreement with the evolution previously noted for the instability strips, since the vertical bifurcations occur at the edges of each strip. Of particular significance are the changes in the characteristic which bifurcates from  $V_1$ , where the extent of stable orbits increases significantly. We also see the creation of a  $2:2_s:1$  (BAN) orbital family, forming a loop between the bifurcation points  $V_3$  and  $V_4$ , respectively on  $x_3$  and  $x_2$ , which grows larger with increasing ring mass. Half the loop, up to the maximum in  $z$ , is stable while the other half is unstable. A family of  $2:2_a:1$  (ABAN) orbits also connects  $S_3$  and  $S_4$  through a bifurcation in  $\dot{z}$  at  $V_7$  and  $V_8$ , but is unstable everywhere, with a section on the high energy side being complex unstable. These non-planar orbits are elongated perpendicular to the bar and connect the planar  $x_2$  and  $x_3$  families.

### 4.3. With an Elliptical Nuclear Ring

To examine the effect of a non-circular ring, we have run models with the maximum ring mass (as in model D), a small eccentricity ( $e = 0.4$ ), and at varying position angles with respect to the bar. We find that for rings which are either aligned with ( $\alpha = 0^\circ$ ) or perpendicular ( $\alpha = 90^\circ$ ) to the bar, the differences with the circular ring are small. The planar characteristics of model D, which has a circular ring, and model E, with the ring major-axis aligned with the bar, differs only in that the “bump” of model E is slightly smoother. For model G, with the ring major-axis aligned perpendicular to the bar, the break in the  $x_1$  characteristic at the high energy side of the “bump” is sharper and the  $x_2/x_3$  loop extends to a slightly lower value of  $E_J$ . A qualitatively different behavior of  $x_1$  and  $x_2$  orbits is obtained when the ring major-axis is oblique to the bar axes.

Unlike stellar orbits, gas orbits are subjected to dissipational processes. This has the effect of broadening the range of orbital frequencies which respond to a resonance. In contrast to the stellar orbits which may abruptly change orientation by  $90^\circ$  at an ILR, the gas orbits make a slower transition. Depending on the details of the potential and pattern speed, the gas may settle in the ILR region on orbits which are neither aligned nor perpendicular to the bar, but instead at some intermediate angle.

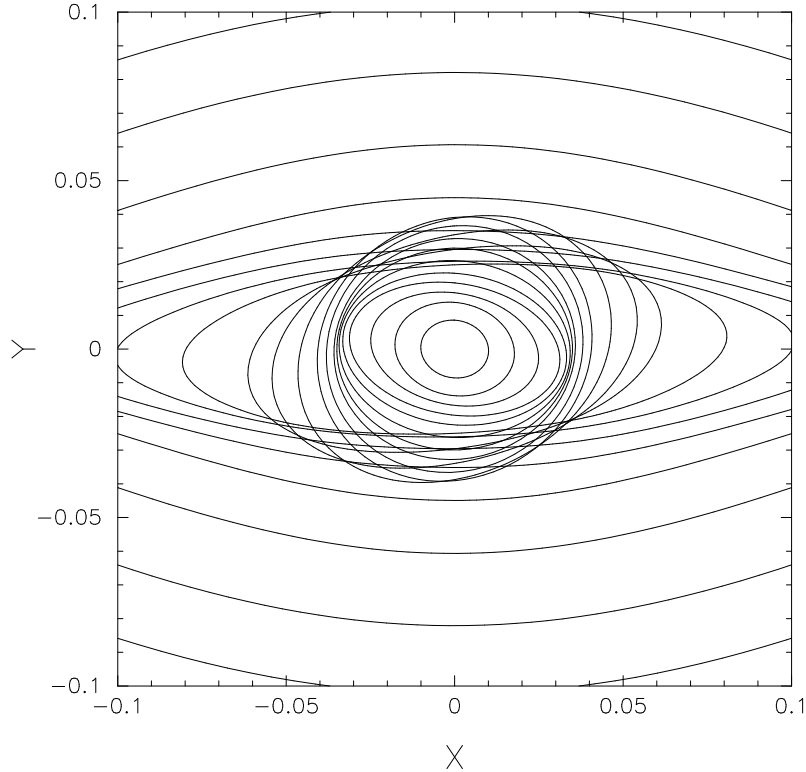


Fig. 10.— Twisting of  $x_1$  orbits from model F with oblique elliptical ring. The ring with an ellipticity of  $e = 0.4$  and semi-major axis  $R_0 = 0.04$  is offset to the bar by  $\alpha = 60^\circ$  in the leading direction. The frame is 2 Kpc on a side.

This configuration is the one typically observed for nuclear rings and also appears as a long-lived transient in our numerical simulations (Knapen et al. 1995a). We investigate this by making the ring major-axis oblique to the bar axes. In this case, we observe that the major-axes of the  $x_1$  orbits become phase shifted, with the position angle of their axes a function of radius. This is shown in Figure 10, where we have plotted some representative  $x_1$  orbits of model F. The change in eccentricity and position angle of the  $x_1$  orbits as a function of their semi-major axis is shown in Figure 11. The models are for a  $10^9 M_\odot$  ring leading the stellar bar by  $60^\circ$  and with eccentricities of 0.0, 0.2, 0.4, and 0.6. The eccentricity of the nuclear ring does show a strong effect on the position angle of the  $x_1$  orbits, both outside and inside the ring (Fig. 11). In addition, the eccentricity of the  $x_1$  orbits interior to the ring is increased with the eccentricity of the ring itself.

The  $e = 0.4$  ring (model F) differs little from the circular ring ( $e = 0.0$ , model D) in the trend of orbit eccentricity with semi-major axis except for a small shift. The eccentricity of model F reaches a maximum of  $e = 0.79$  at  $R = 0.030$  or  $E_J = -6.03$ , followed by a minimum of  $e = 0.37$  at  $R = 0.038$  or  $E_J = -5.72$ . However, the change in the position angle with  $R$  is rather dramatic, starting at large radii with a slowly growing phase shift which reaches a maximum of  $34^\circ$  in the

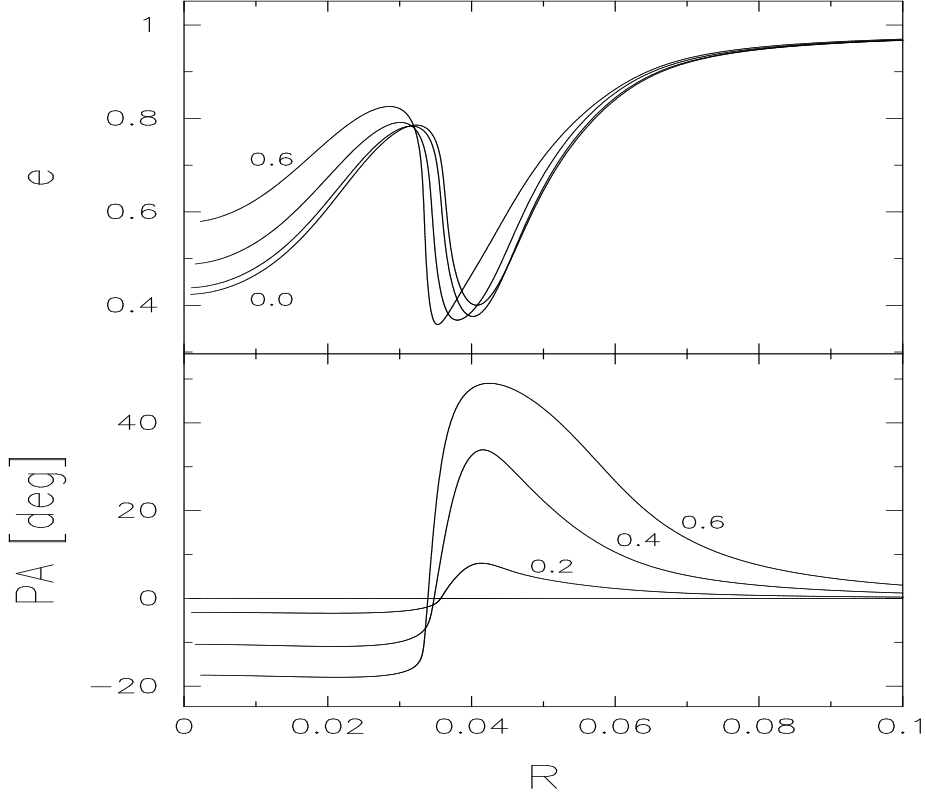


Fig. 11.— Eccentricity and position angle of  $x_1$  orbits as a function of their semi-major axis. The models are for a  $10^9 M_\odot$  ring leading the stellar bar by  $60^\circ$  and with eccentricities of 0.0, 0.2, 0.4, and 0.6.

leading direction at  $R = 0.042$  or  $E_J = -5.61$ , followed by a fast decline to  $0^\circ$  at  $R = 0.035$  or  $E_J = -5.86$ , and then continuing to  $-11^\circ$  in the trailing direction at  $R = 0.021$  or  $E_J = -6.16$ , after which, remarkably, it remains offset in the trailing direction deep into the bulge. As can be seen from the Figure 11, the minimum in eccentricity is slightly offset from the maximum position angle in radius.

This behavior of  $x_1$  orbits can be understood within the framework of forced oscillations. The new thing here is that the orbit is responding to two external forces, the stellar bar and an oblique ring, which have the same driving frequency but are phase-shifted. A straightforward application of the epicyclic approximation (see Appendix A) shows that the main periodic orbits respond by twisting the orientation of their major axes with respect to the stellar bar. Even in the case when the ring is more or less circular, but the mass distribution has a quadrupole moment, should the effect remain qualitatively the same. Further technical details are provided in Appendix A.

## 5. SUMMARY AND CONCLUSIONS

We have performed an orbital analysis in a 3D galactic potential perturbed by a growing nuclear ring. The galaxy consisted of a disk, bulge and a bar. We have studied the effects of circular and oval rings positioned in the preexisting double radial ILR region of this system.

Different orientations of the oval ring with respect to the stellar bar have been tested as well: aligned, perpendicular, and leading by  $60^\circ$  in the direction of galactic rotation. In all cases, both the ring’s semi-major axis and the initial outer radial ILR were smaller than the semi-minor axis of the bar by a factor of  $\sim 3$ . The ring’s mass was always negligible compared to the overall mass of the system, but is responsible for a local distortion of the axisymmetric rotation curve.

We find that the major periodic orbits within the corotation radius are profoundly affected by the perturbation of the ring. For both circular and oval rings we observe a substantial increase in the phase space allowed by the  $x_2$  orbits. If these orbits would be populated, the bar would be weakened. The biggest change comes from the outer radial (and vertical) ILR moving further out to higher energies and increasing its x- and y-extents. The inner ILR moves inwards only slightly. Hence the growing mass in the ring affects mostly the orbits outside the ring (this can be seen even more explicitly in the case of the oblique ring of model F). The only effect the ring has on the inner  $x_1$  orbits is the appearance of a shoulder (bump) interior to the inner ILR in the characteristic diagram (Fig. 3). This reflects the fact that the  $x_1$  orbits in this region become more rounded. Also, the vertical instability strips of the  $x_1$  orbits,  $S_1$  and  $S_2$ , are moving closer to the radial ILRs, i.e. to lower energies. Whereas  $S_1$  becomes narrower,  $S_2$  widens substantially towards lower energies (Fig.3). The  $x_2$  orbits acquire vertical instability strips as well, when the ring becomes massive. This has some similarity to the slowly rotating triaxial models of Udry (1991).

Weakening of the bar, when increasing the central mass concentration in a galaxy by adding a massive BH and/or bulge, was reported in all relevant studies (Pfenniger and Norman 1990; Hasan and Norman 1990; Hasan, Pfenniger & Norman 1993). It was associated with the appearance of a single radial (and vertical) ILR due to the altered rotation curve. This ILR moved out rapidly with the growing central mass  $M_c$ , specifically  $R_{\text{ILR}} \propto M_c^{2.8}$  (e.g. Pfenniger 1996). Under these circumstances, chaotic orbits dominate the space between the center and the ILR, which quickly approaches the semi-minor axis of the bar, causing the dissolution of the stellar bar in a secular process. In addition, higher order radial and vertical ILRs contribute to this effect by widening the resonance zone. The growing central mass repels the  $x_1$  family of orbits from the central region, i.e. within the ILR, and by doing so it also affects the motion out of the xy-plane. This happens because of two reasons (Hasan, Pfenniger and Norman 1993). First, the vertical bifurcation points which mark the origin of 3D orbits, as described in Section 4, move away from the center as the central mass grows. Second, the stability of the out-of-the-plane orbits is affected, with a region of instability appearing in the innermost family of orbits, which corresponds to our  $V_1$  (2:2<sub>s</sub>:1) orbits.

The model presented here differs from the above scenario mainly in two aspects: the

preexisting *double* radial (and a single vertical) ILRs, and the differing symmetry in the perturbing potential, which is far from being spherically-symmetric. Consequently, the  $x_2$  orbits continue to be limited only to the space between the radial ILRs, whereas the  $x_1$  orbits still support the bar between the center and the inner ILR, and between the outer ILR and corotation. This is true irrespective of the ring’s mass, shape or inclination to the bar. The radius of the outer ILR grows approximately *linearly* with the mass in the ring, slower than in the case of the central mass increase. In addition, an oval ring, oblique to the bar, further degrades the symmetry in the galactic plane, which is otherwise dominated by the  $m = 2$  mode due to the stellar bar. As a result the  $x_1$  orbits within  $\sim 2 - 3$  semimajor axes outside the ring, and at the position of the ring, are significantly distorted. We note, that such shapes and inclinations of a ring are not merely of a theoretical possibility, but are in fact supported by observations of molecular gas distributions in nuclear starburst galaxies.

The above differences, between the dynamical effects of a central mass and of a ring, create interesting possibilities for bar evolution in response to the growing mass in the ring. In both cases the stellar bar should weaken as the supporting  $x_1$  family of orbits are destroyed or depopulated. However, the ring has a relatively small effect on the interior orbits, and so we expect that the dissolution of the bar should mainly proceed at and exterior to the ILR resonance region. We speculate, that the observed difference between stellar bars in early and late-type disk galaxies (Elmegreen and Elmegreen 1989) may have its origin in the secular dissolution of the  $x_1$  family of orbits beyond the ILR(s).

Another example which is relevant to this discussion and was studied by us in detail using high-resolution NIR imaging is M100 (=NGC 4321), a nuclear starburst galaxy of intermediate type SABbc (Knapen et al. 1995a,b). This galaxy exhibits all the virtues of a double ILR with a nuclear ring. It possesses a 6 kpc semimajor axis stellar bar, bisected by a weakly oval NIR nuclear ring whose inner boundary, at the inferred position of the inner ILR, is clearly delineated by an incomplete ring of star formation. If NIR isophote ellipse fitting provides a reliable measure of the strength of the barred potential, we measure the maximal ellipticity exterior to the ring to be approximately 20% lower than the maximal ellipticity interior to the ring. It is very interesting, that its NIR isophote twist is similar to that of Fig. 10 (see also Fig. 11). Two more examples supporting our conjecture that nuclear rings weaken mainly the large-scale bars are NGC 4274 and NGC 4643 (Shaw et al. 1995), whose nuclear barlike features have higher ellipticities than their primary bars.

A crude estimate from our model shows that the linearly growing radius of the outer radial ILR will reach the size of the semi-minor axis of the bar when the mass in the ring is approaching  $\sim 10^{10} M_{\odot}$ , a value which is comparable to typical masses of galactic bulges. Evidently, the stellar bar cannot extend to the corotation in this case. Of course, the above model lacks self-consistency in the sense that the orbit analysis is performed in the static potentials of a galaxy and stellar bar. In reality, the stellar bar potential would adjust itself to the loss of the main supporting orbits and the dissolution process would be accelerated, lowering the mass required for bar destruction

between the ILRs and the corotation.

How relevant is the above analysis for the gas evolution in the barred region? Periodic orbits do not exactly correspond to the gas orbits in a galactic potential, mainly due to our neglect of pressure forces. However, by virtue of being the most stable orbits, they can trap gas if the latter is only weakly dissipative. We find that the  $x_1$  periodic orbits of different Jacobi energy in our models begin to intersect in the vicinity of a ring when its mass provides a sufficient perturbation to the background potential. The  $x_2$  orbits start to intersect later-on, when the ring becomes even more massive. This difference in the behavior of  $x_1$  and  $x_2$  orbits happens because the latter are more rounded than the  $x_1$  orbits (see Section 4.1) and must be perturbed stronger in order to overlap. We estimate roughly that this occurs when the mass in the ring approaches  $\sim 10\% - 20\%$  of the mass interior to the ring, and so the self-gravity in the gas cannot be neglected. The above estimate agrees favorably with the results of  $N$ -body simulations (Wada and Habe 1992; Heller and Shlosman 1994; Knapen et al. 1995a). Such intersecting orbits will be quickly depopulated by the gas in a steady state flow which can only move to orbits deeper in the potential well.

An even stronger effect on the gas is expected in the model with an oblique ring (model F). Here the  $x_1$  orbits experience a large-angle rotation with respect to the bar due to the double forcing from the bar and the ring. Such rotations would almost certainly lead to the intersection between  $x_1$  orbits, which exterior to the ring, have fairly eccentric shapes. Stars populating these orbits would contribute to the twisting of isophotes, such as observed in the NIR, in a number of nuclear starburst galaxies (Shaw et al. 1993; Knapen et al. 1995b). If the gas populates these orbits, it will quickly lose angular momentum in shocks and will fall through towards the nonintersecting  $x_2$  orbits (if such exist), where it is expected to accumulate. Knapen et al. (1995a) found that subsequent evolution of this gas depends crucially on its self-gravity, which acts roughly as a surface tension. It causes the gaseous ring to contract by shifting to lower energy  $x_2$  orbits and ultimately shrinking across the inner ILR towards the interior non-intersecting  $x_1$  orbits. Hence, oblique nuclear rings represent transient phenomena. Their characteristic time scales of  $\sim 10^8 - 10^9$  yrs and their potentially recurrent nature make them important when studying gas and stellar dynamics of galactic interiors.

Stability of accumulating gas in the ring, with its self-gravity increasingly dominating the local dynamics, is an important issue. Simulations of such gaseous rings support the above arguments and are capable of following the gas evolution into the nonlinear regime. Knapen et al. (1995a) observed the accumulation of gas at the inner ILR and the beginning of its subsequent collapse to the center. This instability is clearly dynamical, but its growth and the final outcome depends on the efficiency of star formation and the fraction of the released stellar energy (winds and supernovae) which is radiated away by the ISM. Clearly, this phase of evolution in barred galaxies is closely related to their circumnuclear activity and deserves further study. An intriguing possibility is that the gas accumulated in the nuclear rings becomes dynamically unstable by decoupling from the background gravitational potential, leading to a runaway instability and dumping some of this material much closer to the center (Shlosman, Frank and Begelman 1989).

In summary, we have analyzed the main periodic orbits in a barred galaxy perturbed by a massive ring positioned in the inner resonance region, in the vicinity of a double ILR. In some respects, the effect of the ring is similar to that of a central spherically-symmetric mass concentration studied earlier in the literature, such as the secular evolution of the stellar bar. However, a number of profound differences exist. In particular, we find that the orbits affected most are those exterior to the ring, leading to the weakening and ultimate dissolution of the large-scale bar, while the part of the bar interior to the ring and to the ILRs remain stable. It remains to be seen how the proposed evolution of bar length fits the observed difference in bar properties between early and late-type disk galaxies. We also find that oblique rings are capable of inducing an azimuthal twist in the main periodic orbits supporting the stellar bar, similar to that observed in the NIR in some nuclear starburst galaxies. Overall, gas evolution in the vicinity of nuclear rings is accelerated due an increasing number of intersecting orbits there. This underlines the crucial role that self-gravity in the gas plays in driving the circumnuclear activity in barred galaxies.

ACKNOWLEDGMENTS. We have benefited from discussions with Daniel Friedli, Marc Murison and Jerry Sellwood. This work was partially supported by NASA grant NAGW-3839 to the University of Kentucky.

### A. ORBIT RESPONSE TO A DOUBLE PERTURBING FORCE

Applying epicyclic approximation to a particle on a circular orbit with a radius  $R$ , we linearize its equations of motion in analogy with Binney & Tremaine (1987), i.e. the full potential  $\Phi = \Phi_0 + \Phi_1$ , the orbital radius  $R = R_0 + R_1$ , etc. Here subscript ‘0’ refers to unperturbed state and all perturbations are small, i.e.  $\Phi_1/\Phi_0 \ll 1$  and so on. The linearized equations of motion in polar coordinates,  $R$  and  $\theta$ , are given by:

$$d^2 R_1/dt^2 + \left[ (d^2 \Phi_0/dR^2) - \Omega^2 \right]_{R_0} R_1 - 2R_0 \Omega_0 d\theta_1/dt = - (d\Phi_1/dR)_{R_0}, \quad (\text{A1})$$

$$d^2 \theta_1/dt^2 + 2\Omega_0 (dR_1/dt) / R_0 = - \frac{1}{R_0^2} \left[ \frac{d\Phi_1}{d\theta} \right]_{R_0}, \quad (\text{A2})$$

where  $\Omega(R) \equiv \sqrt{(d\Phi_0/dR)/R}$  and  $\Omega_0 \equiv \Omega(R_0)$ . Under *two* periodic perturbing bisymmetric forces having the same frequency but a phase shift, e.g. of a stellar bar and of an oblique massive nuclear ring at an angle  $\alpha$  ( $\leq 90^\circ$ ) to the bar, the perturbing potential can be written as

$$\Phi_1(R, \theta) = \Phi_{\text{bar}}(R) \cos 2\theta + \Phi_{\text{ring}}(R) \cos 2(\theta - \alpha), \quad (\text{A3})$$

where  $\theta(t) = \theta_0(t) \equiv (\Omega_0 - \Omega_{\text{bar}})t$ , in the frame of the bar and  $\Phi_{\text{ring}}$  is the amplitude of the non-axisymmetric part of the ring potential. The solution to the equations (A1-2) in the presence of the perturbing gravitational potential  $\Phi_1$  can be formally written as



$$R_1(\theta_0) = -\frac{1}{\kappa_0^2 - 4(\Omega_0 - \Omega_{\text{bar}})^2} \times \left\{ \left[ \frac{d\Phi_{\text{bar}}}{dR} + \frac{2\Omega\Phi_{\text{bar}}}{R(\Omega - \Omega_{\text{bar}})} \right]_{R_0} \cos 2\theta_0 + \left[ \frac{d\Phi_{\text{ring}}}{dR} + \frac{2\Omega\Phi_{\text{ring}}}{R(\Omega - \Omega_{\text{bar}})} \right]_{R_0} \cos 2(\theta_0 - \alpha) \right\}. \quad (\text{A4})$$

Introducing “effective” radial perturbing forces from a bar and a ring  $F_{\text{eff},i} \equiv -d\Phi_i/dR - 2\Omega\Phi_i/[R(\Omega - \Omega_{\text{bar}})]$ , where  $i = 1, 2$  stand for a *bar* or *ring*, respectively, eq.(A4) can be written as

$$R_1(\theta_0) = \frac{1}{\kappa_0^2 - 4(\Omega_0 - \Omega_{\text{bar}})^2} [F_{\text{eff,bar}} \cos 2\theta_0 + F_{\text{eff,ring}} \cos 2(\theta_0 - \alpha)]. \quad (\text{A5})$$

The orbital response to the double external force of a bar and a ring is equivalent to the response to a *single* force with an amplitude  $F_{\text{eff}}$ , i.e.  $F_{\text{eff}}^2 = F_{\text{eff,bar}}^2 + F_{\text{eff,ring}}^2 + 2F_{\text{eff,bar}}F_{\text{eff,ring}} \cos 2\alpha$ , and with the phase  $\beta$ , given by

$$\beta = \frac{1}{2} \arctan \frac{F_{\text{eff,ring}} \sin 2\alpha}{F_{\text{eff,bar}} + F_{\text{eff,ring}} \cos 2\alpha}. \quad (\text{A6})$$

The equation (A5) can therefore be written in a more compact form,

$$R_1(\theta_0) = \frac{1}{\kappa_0^2 - 4(\Omega_0 - \Omega_{\text{bar}})^2} F_{\text{eff}} \cos 2(\theta_0 - \beta). \quad (\text{A7})$$

We note that  $\beta$  is generally a function of  $R$  and can be both positive and negative depending on the radial change in  $F_{\text{eff,ring}}(R)$  and  $F_{\text{eff,bar}}(R)$ .

## REFERENCES

- Athanassoula, E. 1992, MNRAS, 259, 345  
Athanassoula, E., Bienaymé, O., Martinet, L., & Pfenniger, D. 1983, A&A, 127, 349  
Binney, J. & Tremaine, S. 1987, Galactic Dynamics (Princeton: Princeton Univ. Press)  
Benedict, G.F. et al. 1993, AJ, 105, 1369  
Bosma, A. 1981, AJ, 80, 1825  
Buta, R. & Crocker, D.A. 1993, AJ, 105, 1344  
Combes, F. & Gerin, M. 1985, A&A, 150, 327  
Contopoulos, G. & Papayannopoulos, Th. 1980, A&A, 92, 33  
de Vaucouleurs, G. 1963, ApJS, 8, 31  
Elmegreen, B.G. & Elmegreen, D.M. 1989, ApJ, 342, 677

- Emmering, R.T., Blandford, R.D. & Shlosman, I. 1992, *ApJ*, 385, 460
- Hasan, H. & Norman, C.A. 1990, *ApJ*, 361, 69
- Hasan, H., Pfenniger, D. & Norman, C.A. 1993, *ApJ*, 409, 91
- Heller, C.H. & Shlosman, I. 1994, *ApJ*, 424, 84
- Ferrers, N.M. 1877, *Quart. J. Pure Appl. Math.*, 14, 1
- Friedli, D. & Benz, W. 1993, *A&A*, 268, 65
- Kenney, J.D.P. 1996, in *The Interstellar Medium in Galaxies*, Ed. J.M. van der Hulst (Dordrecht: Kluwer Acad. Publ.), in press
- Kenney, J.D.P., Wilson, C.D., Scoville, N.Z., Devereux, N.A. & Young, J.S. 1992, *ApJ*, 395, L79
- Knapen, J.H., Beckman, J.E., Heller, C.H., Shlosman, I. & de Jong, R.S. 1995a, *ApJ*, 454, 623
- Knapen, J.H., Beckman, J.E., Shlosman, I., Peletier, R.F., Heller, C.H. & de Jong, R.S. 1995b, *ApJ*, 443, L73
- Kormendy, J. 1982, in *Morphology & Dynamics of Galaxies*, Eds. L. Martinet & M. Mayor (Geneva Observatory), p. 155
- Kormendy, J. 1993, in *IAU Symp. 153 on Galactic Bulges*, Eds. H. Habing & H. Dejonghe (Dordrecht: Kluwer Acad. Publ.), p. 209
- MacMillan, W.D. 1958, *The Theory of the Potential*, (New York: Dover Publ.), p. 195
- Martinet, L. 1995, *Fund. Cosmic Physics*, 15, 341
- Martinet, L. & Pfenniger, D. 1987, *A&A*, 173, 81
- Miyamoto, M. & Nagai, R. 1975, *Publ. Astron. Soc. Japan*, 27, 533
- Pfenniger, D. 1984, *A&A*, 134, 373
- Pfenniger, D. 1996, in *IAU Coll. 157 on Barred Galaxies*, Eds. R. Buta et al. (ASP Series), in press
- Pfenniger, D. & Friedli, D. 1993, *A&A*, 270, 561
- Pfenniger, D. & Norman, C.A. 1990, *ApJ*, 363, 391
- Pfenniger, D., Combes, F. and Martinet, L. 1994, *A&A*, 285, 79
- Prince, P.J. & Dormand, J.R. 1981, *Jour. Comp. Appl. Math.*, 7, 67
- Rix, H.-W. & Zaritsky, D. 1995, *ApJ*, 447, 82
- Sellwood, J.A. & Wilkinson, A. 1993, *Rep. Prog. Phys.*, 56, 173
- Shaw, M., Axon, D., Probst, R. & Gatley, I. 1995, *MNRAS*, 274, 369
- Shaw, M., Combes, F., Axon, D.J. & Wright, G.S. 1993, *A&A*, 273, 31
- Shlosman, I. & Noguchi, M. 1993, *ApJ*, 414, 474
- Shlosman, I., Begelman, M.C. & Frank, J. 1990, *Nature*, 345, 679

- Shlosman, I., Frank, J. & Begelman, M.C. 1989, *Nature*, 338, 45
- Telesco, C.M. & Decher, R. 1988, *ApJ*, 334, 573
- Udry, S. 1991, *A&A*, 245, 99
- van Albada, T.S. & Sanders, R.H. 1982, *MNRAS*, 201, 303
- Wada, K. & Habe, A. 1992, *MNRAS*, 258, 82